Journal of RAMAN SPECTROSCOPY

Received: 11 October 2010 Accepted: 24 February 2011

(wileyonlinelibrary.com) DOI 10.1002/jrs.2955

Raman spectroscopy study of damage induced in fluorapatite by swift heavy ion irradiations

S. Miro,[a]* J. M. Costantini,[b] J. F. Bardeau,[c] D. Chateigner,[d] F. Studer[d] and E. Balanzat[e]

Raman spectroscopy was used to study the radiation damage of fluorapatite single crystals and sinters. Krypton and iodine ion irradiations were performed at high energies (∼1 MeV amu^{-1}) for fluences ranging between 1×10^{11} and 5×10^{13} cm^{-2}. Evolution of the symmetric stretching mode of the PO_4^{3-} tetrahedral building blocks (strongest Raman mode observed at 965 cm^{-1}) *versus* ion fluence was investigated. After irradiation, this peak decreases in intensity and a second broader peak appears at lower wavenumber. The well-resolved peak has been assigned to the crystalline phase, and the broader one to the amorphous phase. The integrated intensity ratios of these two peaks *versus* fluence are in good agreement with the damage fractions determined by X-ray diffraction (XRD). Fits of the amorphous fraction *versus* fluence show that the amorphization mechanisms is dominated by a single-impact process for iodine ions and by a double-impact process for krypton ions in the case of single crystals and sinters. For both irradiations, complete amorphization could not be obtained. The amorphous fraction saturates at a maximum value of 88% for sinters and 72% for single crystals. This is attributed to a recrystallization effect which is more important in single crystals than in sinters. For both types of samples, the crystalline peak shifts slightly to a lower wavenumber with fluence, and then shifts back to its initial value for an amorphous fraction larger than 60%. This feature is attributed to a stress relaxation, as shown in the XRD data, which is accompanied by a decrease of the crystalline peak full-width at half-maximum.

Keywords: fluorapatites; swift heavy ion irradiations; Raman spectroscopy

Introduction

Apatites are considered as potential matrices for nuclear waste storage. In its most common high-symmetry representation,[1] apatite is the generic name of a family of calcium phosphates with formula $Me_{10}(XO_4)_6A_2$ that crystallize in the hexagonal system $P6_3/m$ (C_{6h}^2). The Me atoms (Ca^{2+}, Ba^{2+}, etc.) and the XO_4 group (PO_4^{3-}, VO_4^{3-}, etc.) stand for divalent cations and trivalent anions, respectively. The charge is balanced by monovalent anions A (F^-, I^-, etc.). A well-known representative member of the apatite group is calcium phosphate fluorapatite $Ca_{10}(PO_4)_6F_2$. The quasi-compact arrangement of XO_4 ions constitutes the skeleton of the apatitic structure[2] and reveals two types of tunnels. The first tunnel consists of four cations per cell, denoted Me-I, located at the 4f sites with C_3 symmetry. The second tunnel consists of six cations per cell, denoted Me-II, located at the 6 h sites with C_s symmetry. This site is surrounded by six oxygen atoms of the XO_4^{3-} network and one A anion. The XO_4^{3-} ions site is also of C_s symmetry.

The structural flexibility of apatites with substitution explains why the silicate-substituted apatite, also known as britholite, can be used to store trivalent minor actinides (Np^{3+}, Am^{3+}, Cm^{3+}) or fission products (I^-, Cs^+) of ^{235}U. Apatites also exhibit a high chemical stability in slightly alkaline water medium and are stable against radioactive excitations.[3,4]

During long-time storage of nuclear wastes, spontaneous fissions, which occur only for a few elements (Np, U, Pu), are less probable, but result in the production of highly energetic ions (up to 100 MeV) with masses around 100 amu. Hence, during storage, the matrices can be damaged by heavy ions in the electronic energy loss regime.

In a previous paper,[5] we carried out X-ray diffraction (XRD) analysis of $Ca_{10}(PO_4)_6F_2$ sinters irradiated by heavy ions (Kr, I) in order to simulate the damage induced by fission fragments. XRD data analysis showed that different damage mechanisms are taking place with these ions in the electronic stopping power regime.

In this paper, we focus on $Ca_{10}(PO_4)_6F_2$ (fluorapatite) single crystals and sinters irradiated by heavy ions (Kr, I). We study the damage evolution of sinters with micro-Raman spectrometry data and compare them with the previous XRD data.[5] Moreover, micro-Raman spectrometry allowed us to evaluate the damage induced in single crystals (using the same conditions of analysis as for sinters), which is not easily obtainable by XRD.

Experimental

The fluorapatite sinters with formula $Ca_{10}(PO_4)_6F_2$ were synthesized by reactive sintering of the CaF_2, CaO, $Ca_2P_2O_7$ and

---

* Correspondence to: S. Miro, CEA, DEN, SRMP, 91191 Gif-sur-Yvette Cedex, France. E-mail: sandrine.miro@cea.fr

a CEA, DEN, SRMP, F-91191 Gif-sur-Yvette Cedex, France

b CEA, DEN, SRMA, F-91191 Gif-sur-Yvette Cedex, France

c LPEC, Université du Maine, 72085 Le Mans Cedex 9, France

d CRISMAT (CNRS UMR 6508), ENSICAEN, 14050 Caen Cedex, France

e CIMAP, 14076 Caen Cedex 05, France

Table 1. Irradiation parameters for the krypton and iodine ion irradiations: projected range (R_p), longitudinal straggling (ΔR_p), nuclear $(-dE/dx)_n$ and electronic stopping power $(-dE/dx)_e$ at the incident energy (E)

Ion	$^{86}Kr^{21+}$	$^{127}I^{10+}$
E (MeV)	70	120
R_p (μm)	9.4	12.7
ΔR_p (μm)	0.33	0.48
$(-dE/dx)_e$ (keV nm^{-1})	12.7	18.7
$(-dE/dx)_n$ (keV nm^{-1})	5.4×10^{-3}	9.3×10^{-3}

$CaHPO_4$ precursors at the CRISMAT laboratory (Laboratoire de cristallographie et sciences des matériaux). After thorough mixing, the powder was compacted into disks (diameter of 11 mm and thickness of 1 mm) using a pressure of up to 200 MPa. A heat treatment was then applied at 1500 °C for 6 h under nitrogen flow. The studied single crystals are natural minerals from Durango (Mexico) with the following chemical composition: $Ca_{9.83}Na_{0.03}Sr_{0.01}RE_{0.09}(PO_4)_{5.87}(SO_4)_{0.05}(CO_3)_{0.01}(SiO_4)_{0.06}(AsO_4)_{0.01}F_{1.9}Cl_{0.12}(OH)_{0.01}$ (RE, rare earths) measured by Young *et al*.[6] Crystals were cut and irradiated perpendicular to the c-axis.

Before irradiation, single crystals and sinters were annealed at 500 °C for 6 h.[7] This thermal annealing ensures stress relaxation of the layers perturbed by polishing and by desorption of surface atomic layers. Fluorapatite sinters were characterized by various techniques, namely, XRD, energy dispersive spectrometry, and scanning electron microscopy, to check the absence of crystallized impurities in the ceramics.

Samples were irradiated with 70-MeV ^{86}Kr and 120-MeV ^{127}I ions in order to simulate fission fragments of respectively low and high mass at fluences ranging from 1×10^{11} to 5×10^{13} cm^{-2}. The ^{86}Kr ions were provided at the IRRSUD beam line of the GANIL facility (Caen, France), and the ^{127}I ions at the VIVITRON facility (Strasbourg, France). The irradiation parameters are displayed in Table 1.

The Raman investigations were carried out at the LPEC (Laboratoire de Physique de l'Etat Condensé) using a confocal Horiba Jobin-Yvon T64000 spectrometer in the simple spectrograph configuration equipped with a 600 lines mm^{-1} grating coupled to a liquid-N_2-cooled charge-coupled device detector. Raman scattering measurements were performed using the 514.5-nm line from a Coherent Innova Ar–Kr ion laser with an output power of 50 mW. The spectra were collected in the backscattering geometry through the 100× objective of the confocal microscope with a depth resolution better than 2 μm. Thus, the Raman signal were preferentially recorded from the irradiated layers, with thicknesses of about 9.4 and 12.7 μm for Kr and I ion irradiations, respectively (Table 1). Single spectra were recorded with an integration time varying between 40 and 200 s. All spectra were normalized to an integration time of 60 s.

In order to quantify the effect of fluence on the Raman profiles, the spectra were systematically fitted with the fitting module of the LABSPEC Raman spectroscopy software (Jobin-Yvon, Horiba). This fitting code allowed the determination accurately of the position, full-width at half-maximum (FWHM), and integrated intensity of each peak. Pseudo-Voigt functions with the Gaussian parameter (g) varying from 0 to 1 (if $g = 0$, the contribution is Lorentzian; if $g = 1$, the contribution is Gaussian) were used to fit the peaks.

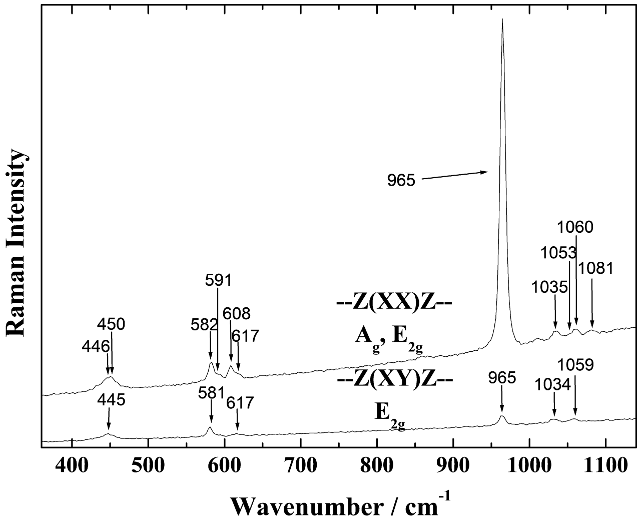

Figure 1. Raman spectra in the Z(XX)Z and Z(XY)Z configurations of a fluorapatite $Ca_{10}(PO_4)_6F_2$ single crystal oriented perpendicular to the *c*-axis.

Theory

An isolated PO_4^{3-} ion exhibits the T_d point symmetry with only four normal modes of vibration: $\nu_1(A_1) = 938$ cm^{-1}, $\nu_2(E) = 420$ cm^{-1}, $\nu_3(T_2) = 1017$ cm^{-1}, and $\nu_4(T_2) = 567$ cm^{-1}. The E and T_2 vibrations are, respectively, doubly and triply degenerate.[8]

In the fluorapatite crystal with the $C_{6h}{}^2$ symmetry, there are six PO_4^{3-} ions per unit cell. The T_d symmetry of a free tetrahedral PO_4^{3-} ion is reduced to C_s in the crystal lattice. This symmetry lowering removes some of the degeneracies of the vibrational wave functions which would have characterized the free PO_4^{3-} ion.

Group theory allows the determination of all the active modes of PO_4^{3-} groups in the crystal.[9,10] There are respectively two, three, and five Raman active modes for A_1, E, and T_2 vibrations. The polarizability tensors for this group are as follows:

$$A_g = \begin{pmatrix} \alpha_{xx} & 0 & 0 \\ 0 & \alpha_{yy} & 0 \\ 0 & 0 & \alpha_{zz} \end{pmatrix}, \quad E_{1g} = \begin{pmatrix} 0 & 0 & \alpha_{xz} \\ 0 & 0 & \alpha_{yz} \\ \alpha_{zx} & \alpha_{zy} & 0 \end{pmatrix},$$

$$E_{2g} = \begin{pmatrix} \alpha_{xx} & \alpha_{xy} & 0 \\ \alpha_{yx} & \alpha_{yy} & 0 \\ 0 & 0 & 0 \end{pmatrix}.$$

A Raman spectrum recorded on the sinters will give directly modes of all symmetry. On the other hand, in the case of single crystals, two directions of polarization noted as Z(XX)Z and Z(XY)Z (using the Porto's notation, (Fig. 1)) will be available in our configuration with the incident beam along the *c*-axis of the crystal. Using this notation, the symbols in brackets are, from left to right, the polarization of the incident and the scattered light, while the ones on both sides of the brackets are the propagation direction of the incident and scattered light, respectively. These polarization directions give access to the symmetries A_g, E_{1g}, and E_{2g}, respectively.

To study the influence of heavy ion irradiation using Raman spectrometry, we focused our study on the most intense peak observed at 965.0 cm^{-1} in single crystals and 967.6 cm^{-1} in sinters.

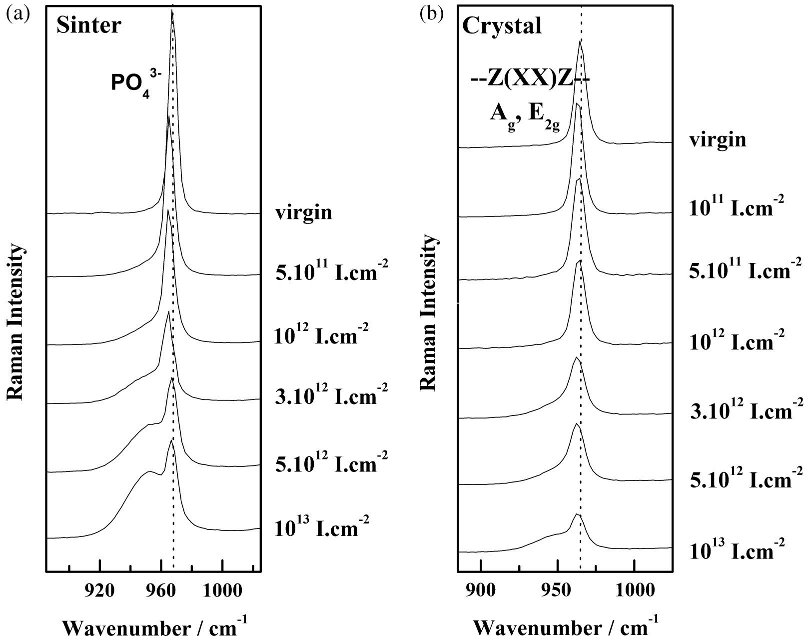

Figure 2. Micro-Raman spectra *versus* fluence for 120-MeV I ion irradiations of (a) sinters and (b) single crystals of $Ca_{10}(PO_4)_6F_2$ fluorapatite.

Data Analysis

An example of variations of the strong peak at 967.6 cm^{-1} *versus* ion fluence for fluorapatite sinters is shown for I ion irradiation in Fig. 2(a). Two contributions are observed: a well-resolved peak which is close to the crystal peak position; and a much broader one which is centered at a lower wavenumber. The narrow crystal-like peaks exhibit Lorentzian shapes, whereas the broader ones show Gaussian shapes. The well-resolved peak decreases in intensity with fluence, and becomes increasingly asymmetrical above 3×10^{12} cm^{-2} for I ion irradiation (Fig. 2a), whereas the second peak is clearly seen to grow with fluence, in agreement with the literature data for Kr and U ion irradiations of Durango fluorapatite single crystal in the gigaelectronvolts energy range.[11]

Moreover, micro-Raman spectrometry allows us to compare the damages induced in fluorapatite single crystals and sintered samples of the same composition. The most intense peak at 965.0 cm^{-1} is displayed at various fluences of I ion irradiation of fluorapatite single crystal in Fig. 2(b). As in the case of sinters, two contributions are observed in the spectra, but the broader one appears clearly only above fluences larger than 1×10^{13} cm^{-2} with smaller intensities than in sinters for the same fluence.

Least-squares fits of the Raman spectra allow us to determine the evolution of fractions of both contributions (integrated intensities) as a function of ion fluence. The fraction of the broader peak (F_a) was then compared with the amorphous fraction deduced from XRD analysis of the irradiated sinters (Fig. 3).[5] For Kr and I ion irradiations, both fractions are in good agreement at all fluences within the experimental error (Fig. 4). We thus assume that the two peaks observed in the micro-Raman spectra can be assigned to the crystalline (for Raman shifts >963 cm^{-1}) and amorphous phases (for Raman shifts <958 cm^{-1}), respectively, as was done in Ref. [11].

For the same fluence, the amorphous fraction (F_a) is larger for I ion irradiation (Fig. 3(b)) than for Kr ion irradiation (Fig. 3(a)), with increasing electronic stopping power. However, at high fluences, the difference in the amorphous fractions between both irradiations is reduced. Plots of the amorphous fraction (F_a) *versus* fluence (ϕ) are least-squares-fitted according to single-impact and double-impact models. We used a modified single-impact model given in Ref. [12]:

$$F_a = F_{sat}(1 - e^{-A\phi}) \qquad (1)$$

where A is the cross section for amorphization, and F_{sat} is the saturation value of the damaged fraction (lower than 100%). The cross section is defined as $A = \pi R_e^2$, where R_e is the effective track-core radius. We also used a modified double-impact model given by the following second-order relation[13]:

$$F_a = F_{sat}[1 - (1 + A\phi)e^{-A\phi}] \qquad (2)$$

In order not to overload the presentation of results, only the best fits of the amorphous fractions are shown (Fig. 3), giving fitted values of A and F_{sat} (Table 2). As in the case of XRD data analysis, the reliability factor χ shows that the double-impact model is the most appropriate for Kr ion irradiation, whereas the single-impact model is the best one for I ion irradiation. A single I ion impact leads to the creation of an amorphous core in latent tracks, whereas a double Kr ion impact is necessary to amorphize the fluorapatite, the first impact giving rise to small 'pre-damaged' domains. The effective radius of amorphization (R_e) for both models increases with increasing electronic stopping power, in agreement with XRD data[5] (Table 2). This confirms that amorphization is enhanced at low fluences with increasing electronic stopping power. For Kr ion irradiation, direct transmission electron microscopy (TEM) observation of incomplete amorphous tracks corresponding to a single impact gave $R_e = 2.05$ nm,[5] which is in fairly good agreement with the single-impact model analysis of the XRD ($R_e = 2.3$ nm) and Raman data ($R_e = 2.5$ nm). The smaller value observed in TEM is probably due to track annealing by electron irradiation, which was already reported in the literature during TEM observations.[14]

For both irradiations, complete amorphization could not be obtained: F_a reaches the saturation values of 82 ± 1 and 88 ± 5%

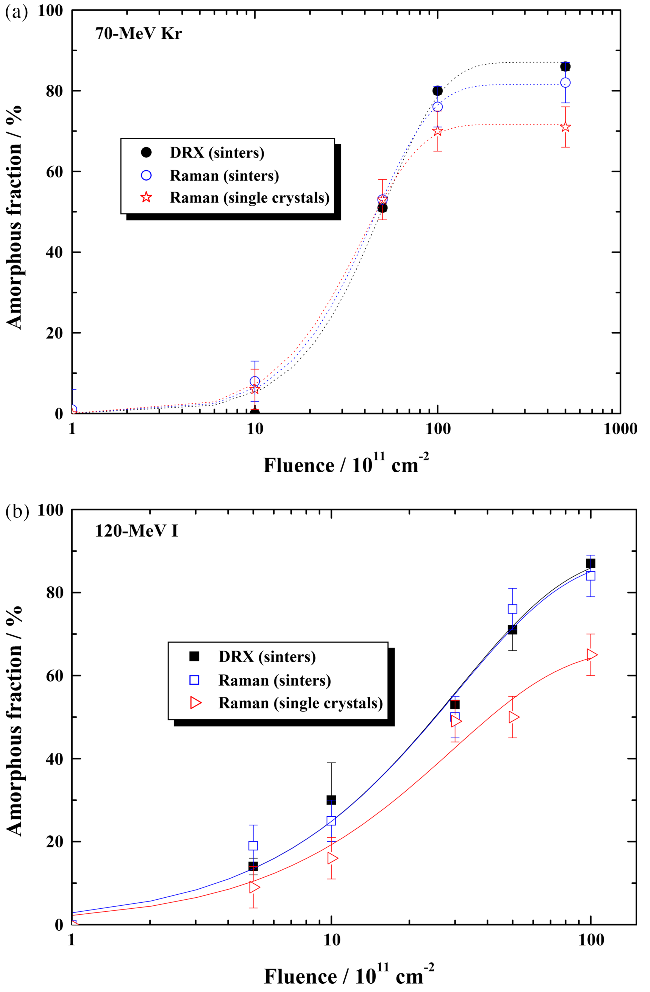

Figure 3. Amorphous fractions *versus* fluence as obtained from micro-Raman spectra of the fluorapatite single crystals and sinters and compared with the data obtained by XRD on sinters.[5] Dashed curves are the best fits using Eqn (2) (double-impact model) for 70-MeV Kr (a) and solid lines using Eqn (1) (single-impact model) for 120-MeV I ion irradiation (b).

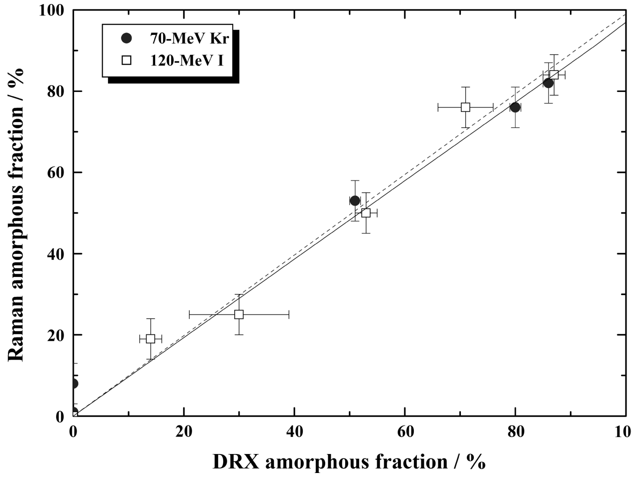

Figure 4. Amorphous fractions deduced from micro-Raman spectra *versus* amorphous fractions deduced from XRD[5] for fluorapatite sinters irradiated with 70-MeV Kr and 120-MeV I ions. The lines are linear regressions of Kr (solid) and I (dashed) ion data.

Table 2. Results of the fits (R_e: effective radius of amorphization, F_{sat}: maximum value of damage of X-ray diffraction (XRD)[5] and micro-Raman spectroscopy data) using the single- and double-impact models (Figs. 3(a) and (b)) for Kr and I ion irradiations with the χ reliability factors of the least-squares fits

Ion	Sample	Technique	Impact	R_e (nm)	F_{sat} (%)	χ
Kr	Sinter	XRD[5]	Single	2.3 ± 0.3	87 ± 9	0.025
			Double	3.5 ± 0.1	85 ± 3	0.003
		Raman	Single	2.5 ± 0.2	84 ± 4	0.007
			Double	3.8 ± 0.1	82 ± 1	0.001
	Single crystal	Raman	Single	2.7 ± 0.3	74 ± 6	0.011
			Double	4.1 ± 0.1	72 ± 1	0.001
I	Sinter	XRD[5]	Single	3.2 ± 0.2	90 ± 4	0.003
			Double	5.4 ± 0.6	80 ± 7	0.032
		Raman	Single	3.2 ± 0.3	88 ± 5	0.009
			Double	5.2 ± 0.5	81 ± 7	0.033
	Single crystal	Raman	Single	3.3 ± 0.3	66 ± 5	0.008
			Double	5.7 ± 0.4	60 ± 3	0.010

for Kr and I ion irradiations, respectively (Table 2). Moreover, the difference between the saturation values is small. This hints that another phenomenon is competing with amorphization at high fluences: this may be the recrystallization process taking place in fluorapatites, in agreement with the defect healing already reported upon α-particle irradiation.[15–17] The saturation values of the amorphous fractions deduced from micro-Raman data are smaller than those determined by XRD data ($F_{sat} = 85 \pm 3\%$ and $F_{sat} = 90 \pm 4\%$ for Kr and I ions, respectively), but the difference lies within experimental errors.

The amorphous fraction is smaller in the single crystals than in sinters at the same fluence, with the difference increasing with fluence (Fig. 3). This effect is seen when considering the maximum value (F_{sat}), which is clearly smaller than that of sinters for both ion irradiations. It seems that the single crystal is damaged to the same level as the polycrystal at low fluences, but that the recrystallization effect is more important in single crystals.

For Kr ion irradiation, the peak position ($\Delta\nu$) and FWHM (Γ) of both contributions vary in the same fashion in single crystals and sinters (Table 3). For I ion irradiation, the effect on $\Delta\nu$ and Γ of the crystal peak is observed at a larger fluence (1×10^{13} cm^{-2}) in single crystals than in sinters, to reach the critical F_a value of $60 \pm 5\%$. For both irradiations of single crystals and sinters, a shift at higher wavenumber close to the initial value is observed for $F_a > 60 \pm 5\%$ (Fig. 5). Indeed, the crystalline phase Raman shift decreases by 1.4 cm^{-1} up to 5×10^{12} cm^{-2} and by 2–3 cm^{-1} up to 3×10^{12} cm^{-2} for Kr and I ion irradiations, respectively, i.e. for $F_a < 60 \pm 5\%$ (Fig. 5 and Table 3). The value of this shift increases with the electronic stopping power. For $F_a > 60\%$, this peak shifts back to the free $PO_4{}^{3-}$ ion values when irradiation proceeds (Fig. 5).

At a fluence of 1×10^{11} cm^{-2}, the FWHM of the crystal peak is smaller than that of the virgin sample, probably due to the initial residual stress relaxation. Then the FWHM increases by ~1–1.4 cm^{-1} with fluence up to 5×10^{12} cm^{-2} and by ~1–1.6 cm^{-1} up to 3×10^{12} cm^{-2} for Kr and I ion irradiations, respectively, i.e. for $F_a < 60 \pm 5\%$, and it decreases for $F_a > 60\%$ (Table 3). The FWHM of the amorphous phase peak, which is about four times as large as that of the crystal, also increases up to 1×10^{13}

Table 3. Raman shifts ($\Delta\nu$) and FWHM (Γ) values of crystalline (denoted as Cryst) and amorphous contributions (denoted as Am) and amorphous fractions (F_a) for sinters and single crystals at various fluences for Kr and I ion irradiations, deduced from the fitting module of the LABSPEC Raman spectroscopy software

Ion	Kr										I									
Sample	Sinter					Single crystal					Sinter					Single crystal				
Fluence (cm^{-2})	$\Delta\nu$ (cm^{-1})		Γ (cm^{-1})			$\Delta\nu$ (cm^{-1})		Γ (cm^{-1})			$\Delta\nu$ (cm^{-1})		Γ (cm^{-1})			$\Delta\nu$ (cm^{-1})		Γ (cm^{-1})		
	Cryst	Am	Cryst	Am	F_a (%)	Cryst	Am	Cryst	Am	F_a (%)	Cryst	Am	Cryst	Am	F_a (%)	Cryst	Am	Cryst	Am	F_a (%)
0	967.6	–	5.7	–	0	965.0	–	7.6	–	0	967.6	–	5.7	–	0	965.0	–	7.6	–	0
1×10^{11}	966.4	–	4.8	–	1	964.0	–	7.5	–	0	–	–	–	–	–	963.4	–	7.4	–	0
5×10^{11}	–	–	–	–	–	–	–	–	–	–	965.4	955.5	6.3	27.1	19	963.9	955.4	8.4	27.0	9
1×10^{12}	966.4	957.6	6.0	26.4	8	964.1	957.8	8.2	27.3	6	965.2	953.6	6.6	28.0	25	964.0	953.6	9.1	27.7	16
3×10^{12}	–	–	–	–	–	–	–	–	–	–	964.6	952.6	6.7	28.1	50	963.0	953.8	9.2	28.2	49
5×10^{12}	966.2	953.0	7.1	27.2	53	963.6	952.9	8.6	27.5	53	967.2	953.5	6.2	28.9	76	963.0	953.7	9.2	28.5	50
1×10^{13}	967.7	953.0	5.4	28.5	76	963.7	951.7	7.7	29.7	70	967.2	952.3	6.2	28.7	84	963.7	951.3	7.9	29.0	65
5×10^{13}	967.1	951.1	4.8	26.5	82	963.7	949.8	7.9	28.9	71	–	–	–	–	–	–	–	–	–	–

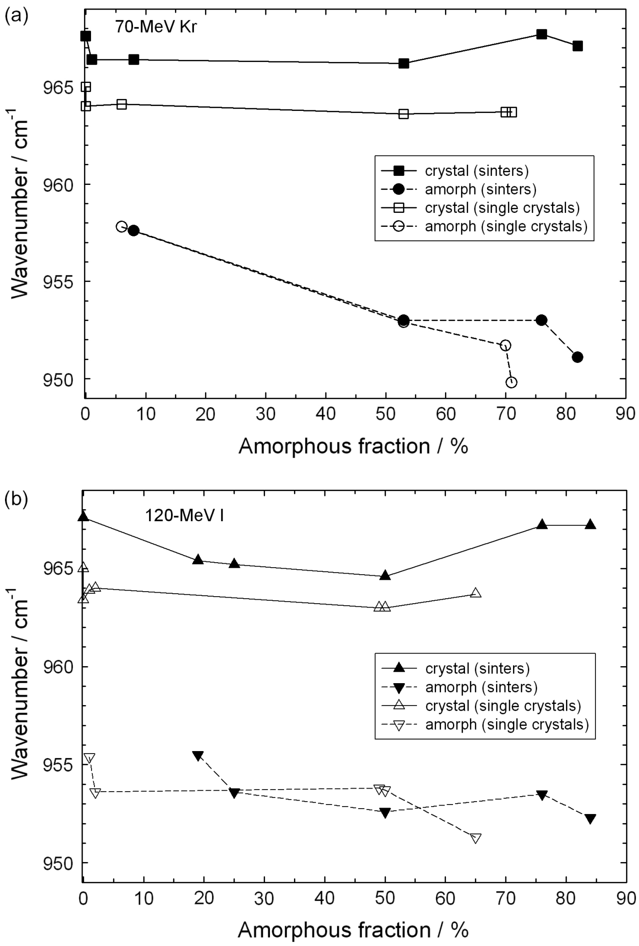

Figure 5. Raman shifts of the crystalline and amorphous phases *versus* amorphous fractions deduced from XRD[5] for fluorapatite sinters and single crystals irradiated with 70-MeV Kr (a) and 120-MeV I (b) ions.

and 5 × 10^{12} cm^{-2} for Kr and I ion irradiations, respectively, and then decreases like the crystal contribution.

These Raman data are consistent with XRD data[5] which show that the unit cell parameters of the crystalline phase shift back to their initial non-irradiated values at high fluences. The increase of F_a is associated with an overall unit cell expansion (swelling) up to a maximum value (which increases with the electronic stopping power) at which the whole material recrystallizes and relaxes into unstrained crystalline and amorphous phases. A similar stress relaxation effect seems to take place in the present Raman scattering spectra.

Discussion

Ab initio calculations of the lattice dynamics of hydroxyapatite ($Ca_{10}(PO_4)_6(OH)_2$) have been performed using the shell model.[18] These calculations show that the phonon bands with wavenumbers below 460 cm^{-1} are due to the mixed vibrational modes of $PO_4{}^{3-}$ groups and Ca^{2+} ions, whereas the phonon bands between 460 and 1200 cm^{-1} are due to the $PO_4{}^{3-}$ vibrations. Comparing the projected and total phonon density of states (DOS) at the Γ-point shows that the major contribution to the optical modes near 900–1000 cm^{-1} comes from P and O atoms, with a very small contribution from the OH^- groups. The Ca atoms contribute only at wavenumbers below 400 cm^{-1}. Other calculations have been performed on hydroxyapatite using a classical potential fitted to *ab initio* data.[19] The calculations of phonon frequencies at the Γ-point confirm that the Raman active modes (with symmetries A, E_1, E_2) between 981 and 989 cm^{-1} correspond to the P–O vibrations. Similar features are expected in the fluorapatites with the same oscillator masses.

It is reasonable to assume that the tetrahedral building blocks ($PO_4{}^{3-}$ groups) of the crystalline fluorapatite phase are conserved at a local scale in the disordered (amorphous) phase due to the strong sp^3 P–O bonding. Actually, electronic structure calculations indicate that the Ca–O bonding in crystalline apatites is highly ionic whereas the P–O bonds in the $PO_4{}^{3-}$ groups are strongly covalent.[20] Therefore, it can be assumed that the broad peak in the Raman spectra is related to an individual P–O vibrational mode in the $PO_4{}^{3-}$ groups in the amorphous phase, whereas the narrow peak is related to the same mode in the crystalline phase. A distribution of the frequencies of these modes, linked to a random distribution of bond lengths and bond angles in the short-range order, induces an inhomogeneous broadening of the Raman peak with a Gaussian shape. However, one cannot neglect the other contributions to the broadening arising from a decrease of lifetime of phonons in finite disordered domains as well as from fluorine vacancies (F-centers) produced by irradiation.[21]

Assuming small differences of polarizabilities and Raman shifts of P–O bonds in the tetrahedral PO_4^{3-} building blocks between the crystalline and amorphous phases, the ratio of intensities of a given mode for the two phases is thus proportional to the ratio of the densities of P–O bond scatterers and, thus, to the ratio of volume fractions of both phases. In this specific case, it is thus possible to extract the damage fraction from the Raman data by using the ratio of the two contributions assigned to the crystalline and amorphous phases.

Further, it is well known that the classical selection rules of periodic solids using the lattice vibration wave vector break down in a disordered solid.[22] In a crystalline solid, the Raman scattering intensity of a given vibration mode corresponds to the folded vibrational DOS for zero optical phonon wave vector (q) at the Γ-point.[23] Therefore, in the amorphized solid, the DOS at $q = 0$ may involve contributions of vibration modes with different symmetry labels from other points of the Brillouin zone. In principle, this makes it difficult to monitor the decrease of long-range order by the decrease of a given Raman peak intensity owing to the overlap of these contributions at the same phonon energies (i.e. same Raman shifts).

However, owing to the weak q-dependence of the Raman active optical modes, it is expected that the disorder-induced shift and broadening of the peak centered at $\sim$965 cm^{-1} arise mostly from the contribution of the PO_4^{3-} groups to the phonon DOS at the Γ-point and not from Ca^{2+} ions in the skeleton, like in the crystalline phase.[18,19] This is consistent with the very good agreement between the amorphous fractions deduced from Raman spectroscopy data and from XRD data on irradiated sinters. This allows measuring quantitatively the damage in single crystals with Raman spectroscopy, whereas it is quite difficult to do so with XRD. This has a very interesting application in monitoring the damage in this material as a host of radioactive wastes. The amorphous fraction is actually increasing with the electronic stopping power in agreement with TEM data and follows a saturation behavior with fluence. The amorphous track-core radii deduced from the saturation curves are also in relatively good agreement with the TEM data.[5]

The evolution of Raman peaks confirms that the recrystallization effect is increasing with fluence and electronic stopping power, as seen with the XRD data, with stress relaxation occurring above a critical amorphous fraction (F_a) of about 60%. This is a remarkable property of damage annealing in this material induced by the electronic excitations, which has strong consequences for the use of this material as a host for nuclear waste management.

Conclusions

Raman spectroscopy analysis of fluorapatite single crystals and sinters irradiated with 70-MeV Kr and 120-MeV I ions shows that the evolution of the radiation damage can be studied with this technique. Indeed, the evolution of the damage fraction *versus* fluence is in good agreement with previous XRD data. The present Raman data confirm that the amorphization mechanism is dominated by a single-impact process for I ions and a double-impact process for Kr ions both in cases of single crystals and sinters. The amorphous fraction increases with the electronic stopping power for a given fluence. Yet, at high fluences, the difference of amorphous fractions between both ion irradiations is reduced with a saturation value of 88% for sinters. At high fluences, the recrystallization effect competes with the damage process, and seems to increase with the electronic stopping power. Finally, Raman spectroscopy was used to compare the evolution of the amorphous fractions in sinters and single crystals. It is found that the amorphous fraction saturates at a lower value (72%) and lower fluences in single crystals due to a stronger recrystallization effect.

Acknowledgement

The authors are indebted to M. Toulemonde (CIMAP, Caen) for fruitful discussions.

References

[1] C. Rey, *Actual. Chim.* **1995**, *7*, 41.
[2] J. C. Elliot, *The crystallographic structure of dental enamel and related apatites*, London University Thesis, **1964**.
[3] R. C. Ewing, L. M. Wang, R. J. Weber, *Mat. Res. Soc. Proc.* **1995**, *373*, 127.
[4] L. M. Wang, M. Cameron, W. J. Weber, K. D. Crowley, R. C. Ewing), in *Hydroxyapatites and Related Materials*, (Eds: P. W. Brown, B. Constantz), CRC Press: Boca Raton, **1994**, pp 243.
[5] S. Miro, D. Grebille, D. Chateigner, D. Pelloquin, J. P. Stoquert, J. J. Grob, J. M. Costantini, F. Studer, *Nucl. Instr. Meth. B.* **2005**, *227*, 306.
[6] E. J. Young, A. T. Myers, E. L. Munson, N. M. Cowklin, Mineralogy and Geochemistry of Fluorapatite from Cerro de Mercado, Durango, Mexico, U.S. Geol. Survey Prof. Paper 650. **1969**, 84.
[7] F. Villa, *Study of the structural evolution of latent fission tracks in apatite during a thermal annealing. Development of a chemical etching simulation*, Franche-Comté University Thesis, **1997**.
[8] W. P. Griffith, *Nature* **1969**, *224*, 264.
[9] L. C. Kravitz, J. D. Kingsley, E. L. Elkin, *J. Chem. Phys.* **1968**, *49*, 4600.
[10] C. Meegoda, C. E. Bonner, G. Loutts, S. Stefanos, G. E. Miller, *J. Lumin.* **1999**, *81*, 101.
[11] J. Liu, U. A. Glasmacher, M. Lang, C. Trautmann, K. O. Voss, R. Neumann, G. A. Wagner, R. Miletich, *Appl. Phys. A* **2008**, *91*, 17.
[12] J. F. Gibbons, *Proc. IEEE* **1972**, *60*, 1062.
[13] C. Gibert-Mougel, F. Couvreur, J. M. Costantini, S. Bouffard, F. Levesque, S. Hémon, E. Paumier, C. Dufour, *J. Nucl. Mater.* **2001**, *295*, 121.
[14] A. Meldrum, L. A. Boatner, R. C. Ewing, *Mater. Res. Soc. Symp. Proc.* **1997**, *439*, 697.
[15] S. Ouchani, J. C. Dran, J. Chaumont, *Nucl. Instr. Meth. B* **1997**, *132*, 447.
[16] S. Soulet, J. Carpéna, J. Chaumont, O. Kaitasov, M. O. Ruault, J. C. Krupa, *Nucl. Instr. Meth. B.* **2001**, *184*, 383.
[17] J. Chaumont, S. Soulet, J. C. Krupa, J. Carpena, *J. Nucl. Mater.* **2002**, *301*, 122.
[18] L. Calderín, D. Dunfield, M. J. Stott, *Phys. Rev. B.* **2005**, *72*, 224304.
[19] A. Pedone, M. Corno, B. Civalleri, G. Malavasi, M. C. Menziani, U. Segre, P. Ugliengo, *J. Mater. Chem.* **2007**, *17*, 2061.
[20] P. Rulis, L. Ouyang, W. Y. Ching, *Phys. Rev. B.* **2004**, *70*, 155104.
[21] W. W. Piper, L. C. Kravitz, R. K. Swank, *Phys. Rev.* **1965**, *138A*, 1802.
[22] S. R. Elliott, *Physics of Amorphous Materials* (2nd edn) Longman: Harlow, **1990**.
[23] C. Kittel, *Introduction to Solid State Physics*, (6th edn) Wiley: New York, **1986**.